

Research Article

A Novel Neutrosophic Method for Automatic Seed Point Selection in Thyroid Nodule Images

S. O. Haji  and R. Z. Yousif

Department of Physics, College of Science, Salahaddin University, Hawler, Iraq

Correspondence should be addressed to S. O. Haji; salih_omer@yahoo.com

Received 3 December 2018; Accepted 19 March 2019; Published 10 April 2019

Academic Editor: Takashi Saku

Copyright © 2019 S. O. Haji and R. Z. Yousif. This is an open access article distributed under the Creative Commons Attribution License, which permits unrestricted use, distribution, and reproduction in any medium, provided the original work is properly cited.

The thyroid nodule is one of the endocrine issues caused by an irregular cell development. This rate of survival can be improved by earlier nodule detection. Accordingly, the accurate recognition of the nodule is of the utmost importance in providing powerful results in building the survival rate. The reduction in the accuracy of manual or semiautomatic segmentation methods for thyroid nodule detection is due to many factors, basically, the lack of experience of the sonographer and latency of operation. Most lesion regions in ultrasound images are homogeneous. Therefore, the value of entropy in these regions is high compared to its neighbours. Based on this criterion, a novel procedure for automatically selecting the seed point in thyroid nodule images is proposed. The proposed system consists of three components: neutrosophic image enhancement and speckle reduction to reduce speckle noise and automatic seed selection algorithm extracted from the centre of candidate block in ultrasound thyroid images based on the principle that most of its Higher Order Spectra Entropies (HOSE) from Radon Transform (RT) at different angles are within the range between average and maximum entropies, and the region growing image segmentation is applied with the constant threshold. The performance of proposed automatic segmentation method is compared with other methods in terms of calculating, True Positive (TP) value ($96.44 \pm 3.01\%$), False Positive (FP) value ($3.55 \pm 1.45\%$), Dice Coefficient (DC) value ($92.24 \pm 6.47\%$), Similarity Index (SI) ($80.57 \pm 1.06\%$), and Hausdroff Distance (HD) (0.42 ± 0.24 pixels). The proposed system can be considered as an added value to the malignancy diagnosis in thyroid nodule by an endocrinologist.

1. Introduction

Thyroid nodule malignancy is one of the vital life-threatening issues that occurred due to irregular growth of cells that might be benign or malignant [1]. As categorized by American Cancer Society's evaluations for thyroid malignancy in 2018, out of 53,990 new instances of thyroid cancer, 13,090 were males and 40,900 were females in the United States [2].

For an endocrinologist, the basic problem is to physically identify the exact thyroid nodule in the ultrasound image and classify it as benign or malignant [3]. Computer-aided detection frameworks are becoming increasingly popular and help endocrinologists make accurate decisions to understand an enormous amount of image information [4]. One of the main difficulties to be considered in designing a fully computerized recognition framework is the accurate representation of nodules with automatic extraction of the region of interest

(ROI) within the thyroid organ. Alternative difficulties are speckle noise suppression in ultrasound images which was addressed in this study.

Koundal et al. [5] in 2018 utilized full automated computer-aided detection framework for speckle reduction and segmentation of nodules from thyroid ultrasound images. Speckle is an unfortunate obstruction impact, happening when at least two ultrasound waves interfere with each other, constructively or destructively, producing bright and dark spots [6]. For preprocessing of ROI speckle reducing anisotropic diffusion (SRAD) filter has been used by Yu et al. [7]. SRAD is a filter, which iteratively reduces speckle noise, preserves edges, and simultaneously enhances the contrast of the image.

In recent decades, further studies have been carried out to remove speckle noise, e.g., the nonlocal means (NLM) filter utilized by Avazpour 2009 [8] and anisotropic diffusion

(SRAD) filter proposed and created by Mat Isa et al., 2006 [9].

Recently, numerous researchers have used neutrosophy in various applications such as image noise reduction and segmentation, which have shown that the theory of neutrosophy provides a good execution due to its indeterminacy and performance [10–13].

The proposed technique of thyroid nodule summation is mainly based on entropies derived after the application of radon transformation using HOS. Its spectra sometimes referred to as poly-spectra are spectral representations of higher order statistics, i.e., moments, and cumulated by third order and beyond. HOS was first applied to real signal processing problems in 1970. It may be more advantageous to analyze biomedical signals because it is nonlinear, non-stationary, and non-Gaussian [14]. HOS has been applied to various applications, for instance, 1D pattern recognition [15], array signal processing [16], and ultrasound image processing [17].

A seed is a test pixel with a perfect trademark that belongs to the suspicious region and ought to be the piece of the region of interest [18]. Since the region growing outcome is delicate to the underlying seeds, the precise seed choice is essential for image segmentation [19].

Segmentation is a standout of the most troublesome and essential assignments in medical image processing. This dynamic field of research throughout the most recent two decades makes a basic organization or format of the medical image, to indicate a region of interest (ROI). Segmentation is the way toward apportioning image into a few areas as per particular standards. The reason for segmentation is utilizing these regions for ROI detection to recognize any irregularities or lesions. Nature of segmentation decides the possible achievement or disappointment of the investigation or analysis.

Segmentation of medical images utilizing seeded region growing (SRG) procedure is progressively turning into a well-known technique as a result of its capacity to include abnormal state information of anatomical structures in seed choice process [20]. Poonguzhali and Ravindran [21] depict a fully automatic technique for segmentation of masses on ultrasound images by utilizing region growing technique. In their work, the region growing begins by selecting a seed pixel, followed by adding new pixels to the segment (augmented fragment) until the segmentation standard is fulfilled [22]. Seeded region growing has the benefit of indicating only one interested region by putting a seed in it. Be that as it may, the execution of SRG calculations relies on this position.

Various works can be discovered with respect to automatic seed selection. Michahial et al. [23] proposed a technique to calculate and recognize the seed point automatically by which automatic contour initialization is done. Chang et al. in 1994 [24] and Avazpour et al. in 2009 [8] pointed out how the Histogram Feature technique can be used in seeded selection based on feature extraction approach. Mat Isa et al. in 2006 [9], Saad et al. in 2012 [25], and Al-Faris et al. in 2014 [26] utilized moving K-means technique for seeding selection based on region extraction, respectively. On the other hand,

Mustafa et al. in 2010 [27] used active contour model for seed selection based on edge extraction approach.

The idea presented in this work is to identify a seed pixel from the abnormal regions based on entropy capability in differentiating between nonhomogeneous and homogeneous regions in ultrasound images. The previous techniques were depending on entropies derived from spatial domain [21]. HOS is employed as a nonlinear method that helps to capture the subtle changes in pixels of the image and hence to identify the seed point. It was noticed that HOS methods would be a superior methodology than the conventional time domain and frequency domain methods in analyzing the biosignals. It is a great apparatus for the nondirect dynamical investigation of the biomedical signals, so as the case it can battle commotion and give great outcomes even with the case it can combat noise and give good results even with weak signals. In another place, HOS is valuable in recognizing nonlinear coupling and deviation from Gaussianity and features obtained from it tend to be made invariant to move, rotation, and enhancement. The new approach in this research is to depend on the important entropies' values, namely, phase entropy and bispectrum entropies using HOS, these parameters can be used to select a suitable seed pixel from the suspicious regions. The proposed system is beginning with applying Radon transform to each image block; then HOS based entropies values extracted from different ultrasound image resulting from blocks at different orientations (angles) were carried out. Finally, we select the center of candidate block for which most of its entropy's features are high (above the average value derived from all blocks). The spectral entropies are high for a homogeneous region of the possible lesion and low for nonhomogeneous regions. These feature scans are explored for numerous healthcare applications.

2. Materials and Methods

2.1. Dataset. The ultrasound image dataset has been utilized in this paper to compute the efficiency of proposed segmentation method from the open access Digital Database of thyroid ultrasound images from the Universidad Nacional de Colombia Laboratory [28]. It consists of 92 thyroid ultrasound images, out of which 50 were males and 42 were females with various ages. The images were extracted from thyroid ultrasound video sequences captured with a TOSHIBA linear transducer. Thyroid nodules images are saved in ultrasonography system that includes a complete annotation and diagnostic description of suspicious thyroid lesions, using the TI-RADS lexicon description performed by at least two expert radiologists.

2.2. Pre-Processing

2.2.1. Image Enhancement and Sharpening. The principal goal of an image enhancement is to draw out the hidden image details or to expand the image contrast from another powerful range [29]. Neutrosophic based image enhancement is used in this research. Neutrosophy is a part of philosophy displayed in [30] as a generalization of dialectics and studies

the origin, nature, and extent of neutralities, close to their interactions with different ideational spectra. In neutrosophy hypothesis, only one out of every event has a specific level of reality, in addition to a misrepresentation degree and an indeterminacy degree that must be considered uninhibitedly from each other.

(1) *The Image in Neutrosophic Set.* Assume U is a universe of discourse and W is an arrangement of U , which is made by bright pixels. A neutrosophic image PNS is described by three participation sets T, I, F . A pixel P in the image is described as $P(T, I, F)$ and related to W in an accompanying way: It is t , true, in the set, i , indeterminate in the set, and f , false, in the set, where t varies in T , i varies in I , and f varies in F . The component pixels' functions TC, IC , and FC are calculated to transform image from gray-level domain to neutrosophic domain. The participant functions as mentioned before are computed [31], as shown below:

$$TC = \frac{\hat{q}_{ij} - \hat{q}_{\min}}{\hat{q}_{\max}} \quad (1)$$

where i varies from 0 to $n-1$, j varies from 0 to $m-1$, \hat{q}_{ij} is the local mean obtained using a window, \hat{q}_{\min} is the minimum grey level value, and \hat{q}_{\max} is the maximum grey level value.

$$\hat{q}_{ij} = \frac{1}{w \times w} \sum_{m=i-w/2}^{i+w/2} \sum_{n=j-w/2}^{j+w/2} q_{mn} \quad (2)$$

where q_{mn} is the noisy image and w is the size of the window.

$$IC = \frac{\delta_{ij} - \delta_{\min}}{\delta_{\max}} \quad (3)$$

$$\delta_{ij} = \text{abs}(q_{ij} - \hat{q}_{ij}) \quad (4)$$

where δ_{ij} is the absolute value of the difference between intensity q_{ij} and its local mean value \hat{q}_{ij} . The false component in the neutrosophic domain is calculated as

$$FC = 1 - TC \quad (5)$$

(2) *Map Image and Decide $\{T, F\}$.* Consider an image A , $P(x, y)$ is a pixel in the image, and (x, y) is the position of this pixel. A 5x5 mean filter (the size of filter may fluctuate contingent upon the measure of the input image) is applied to A to evacuate noise and make the image uniform. Next, the image is changed by utilizing the S-function:

$$T(x, y) = S(g_{xy}, a, b, c) = \begin{cases} 0 & 0 \leq g_{xy} \leq a \\ \frac{(g_{xy} - a)^2}{(b - a)(c - a)} & a \leq g_{xy} \leq b \\ 1 - \frac{(g_{xy} - c)^2}{(c - b)(c - a)} & b \leq g_{xy} \leq c \\ 1 & g_{xy} \geq c \end{cases} \quad (6)$$

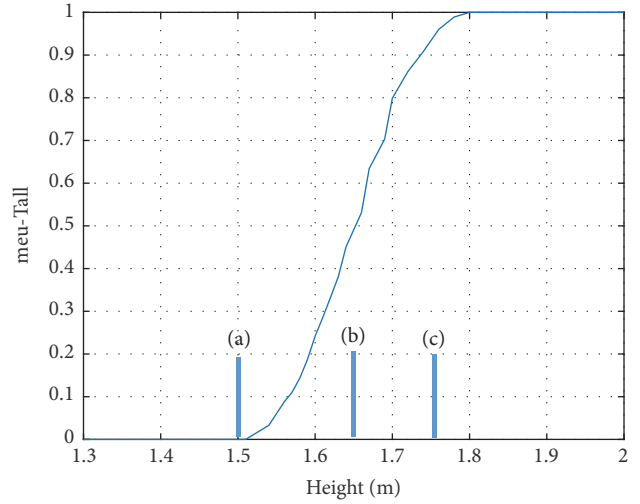


FIGURE 1: S-function.

where g_{xy} is the intensity value of pixel $P(i, j)$. Factors a, b , and c are the parameters that evaluate the state of the S-function as appeared in Figure 1.

Estimations of parameters a, b , and c can be computed by utilizing the simulated annealing method [32]. However, the simulated annealing algorithm is quite time-consuming. Thus, we utilize another histogram-based technique to compute a, b , and c [33].

(1) Calculate the histogram of the image.

(2) Find the local maxima of the histogram: $His_{\max}(g_1), His_{\max}(g_2), \dots, His_{\max}(g_n)$.

Calculate the mean of local maxima:

$$\overline{His_{\max}(g)} = \frac{\sum_{i=1}^n His_{\max}(g_i)}{n} \quad (7)$$

(3) Find the peaks greater than $\overline{His_{\max}(g)}$; let the first peak be g_{\min} and the last peak be g_{\max} .

(4) Define low limit B_1 and high limit B_2 :

$$\sum_{i=g_{\min}}^{B_1} His(i) = f_1 \quad (8)$$

$$\sum_{i=B_2}^{g_{\max}} His(i) = f_1$$

where the data misfortune is permitted in the range $[g_{\max}, B_1]$ and $[B_2, g_{\min}]$, which is in f_1 ($f_1=0.01$ in the experiments).

(5) Compute a and c :

$$a = (1 - f_2)(g_1 - g_{\min}) + g_{\min} \quad (9)$$

$$\text{if } (a > B_1) \text{ then } a = B_1$$

$$c = f_2(g_{\max} - g_n) + g_n \quad (10)$$

If $(c > B_2)$, then $c = B_2$, where $f_2=0.01$, and B_1 and B_2 are utilized to keep away from imperative data misfortune. The intensity less than B_1 is considered as background, and the intensity more than B_2 is considered as noise.

(6) Compute parameter b by utilizing the most extreme entropy central [34].

$$H(x) = \frac{1}{M \times N} \sum_{i=1}^M \sum_{j=1}^N S_n(T(x, y)) \quad (11)$$

where S_n is a Shannon function defined as

$$S_n(T(x, y)) = -T(x, y) - (1 - T(x, y)) \log_2(1 - T(x, y)) \quad (12)$$

$$x = 1, 2, \dots, M, \quad y = 1, 2, \dots, N$$

The maximum entropy principle expresses that the more noteworthy the entropy is, the more data the framework includes [35]. To determine the optimal b try every $b \in [a + l, c - l]$. The optimal b will produce the largest $H(X)$:

$$H_{\max}(X, a, b_{opt}, c) = \max \{H[X; a, b, c] \mid g_{\min} \leq a < b < c \leq g_{\max}\} \quad (13)$$

After a , b , and c are calculated, the image can be mapped from the intensity domain g_{xy} to the new domain $T(x, y)$. Use intensification transformation to enhance the image in the new domain [36]:

$$E(T(x, y)) = 2T^2(x, y) \quad 0 \leq T(x, y) \leq 0.5$$

$$E(T(x, y)) = 1 - 2(1 - T(x, y))^2 \quad 0.5 < T(x, y) \leq 1 \quad (14)$$

Then image sharpening stage involves applying unsharp mask [36] image sharpening technique on the output of image enhancement stage.

2.2.2. Speckle Noise Reducing (SRAD). SRAD is a type of filters generally utilized for removing speckle noise in ultrasound images and it can save edges, as well as enhances edges. SRAD is a Partial Differential Equation (PDE) that had been adjusted by Yu and Action [7] from anisotropic diffusion filter to fit the speckle noise produced by the ultrasound image. In this algorithm, Instantaneous Coefficient of Variation (ICOV) is utilized to separate the edge regions in the image. ICOV is given by

$$q(x, y; t) = \sqrt{\frac{(1/2)(\nabla I/I)^2 - (1/16)(\nabla^2 I/I)^2}{[1 + (1/4)(\nabla^2 I/I)^2]}} \quad (15)$$

where ∇ and ∇^2 denote the gradient and the Laplacian, separately.

$$\nabla_g I_{i,j}^n = \left[\frac{I_{i+1,j}^n - I_{i,j}^n}{h}, \frac{I_{i,j+1}^n - I_{i,j}^n}{h} \right] \quad (16)$$

$$\nabla_L I_{i,j}^n = \left[\frac{I_{i,j}^n - I_{i-1,j}^n}{h}, \frac{I_{i,j}^n - I_{i,j-1}^n}{h} \right] \quad (17)$$

$$\nabla^2 I_{i,j}^n = \left[\frac{I_{i+1,j}^n + I_{i-1,j}^n + I_{i,j+1}^n + I_{i,j-1}^n - 4I_{i,j}^n}{h} \right] \quad (18)$$

ICOV indicate the high value in the edge region and low value in the homogeneous region.

$$C(q) = \frac{1}{(1 + [q^2(x, y; t) - q_o^2(t)]) / [q_o^2(t)(1 + q_o^2(t))]} \quad (19)$$

where $q_o(t)$ is the scale factor of speckle utilized in the dispersion coefficient $C(q)$. Equation (19) controls the measure of smoothing in the homogeneous region (17). In this manner, the speckle scale function removes the noise from the homogeneous region.

$$q_o(t) = \sqrt{\frac{\text{Var}[Z(t)]}{\overline{Z(t)}}} \quad (20)$$

where $\text{Var}[Z(t)]$ and $\overline{Z(t)}$ denote the intensity variance and mean over a homogenous region at t .

2.3. Seed Point Generation Stage. This stage is started by dividing the thyroid ultrasound nodule images into nonoverlapped square blocks of size 11 by 11 pixels. The Radon transform and HOS were implemented on each block separately to calculate 3rd order entropies at different angles.

2.3.1. Radon Transform. Radon transform is generally utilized in processed tomography to make an image from the dispersing information related to cross-sectional outputs of an object. It transforms the two-dimensional images with lines into a domain of possible line parameters, where each line in the image will give a pinnacle situated at the comparing line parameters [37]. Subsequently, the lines of the images are transformed into the points in the Radon domain. An equation of the line can be expressed as

$$r = x \cos \theta + y \sin \theta \quad (21)$$

where θ is the small angle and r is the small distance to the origin of the coordinate system. Given a function $g(x, y)$, Radon transform is defined as

$$R(r, \theta) = \int_{-\alpha}^{+\alpha} A(r \cos \theta - s \sin \theta, r \sin \theta + s \cos \theta) ds \quad (22)$$

Equation (22) depicts the vital along a line through the image, where r is the distance of the line from the origin and θ is the angle from the horizontal. So, radon transform changed 2D signal into the 1D parallel beam projections, at different angles θ .

2.3.2. Higher Order Spectra Entropy (HOSE). Higher request spectra are nondirect strategies, characterized to be spectral representations of higher request cumulants (i.e. c_1 , c_2 , and c_3) of a random process [14]. Both amplitude and phase information for a given signal appear.

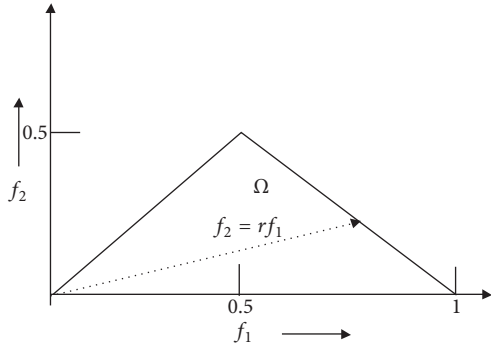


FIGURE 2: The bispectrum for real signal.

The mean value (m) and variance (σ_R^2) are computed by utilizing second-order statistics. They are described by expectation operation as

$$m_r = E [R] \tag{23}$$

$$\sigma_R^2 = E [(R - m_r)^2] \tag{24}$$

where r is a discrete time signal, and the second-order moment autocorrelation function can be defined as

$$m_r^2(i) = E [R(n) \cdot R(n + i)] \tag{25}$$

Thus, HOS is composed of moment and cumulant spectra. They are utilized for both deterministic signals and random processes [38]. The third- and fourth-order cumulant spectra are characterized as bispectrum and the trispectrum, respectively [14].

Bispectrum is the Fourier transform of the third order correlation of the data utilized in this work to determine the features is given by

$$B(f_1, f_2) = E [R(f_1)R(f_2)R^*(f_1 + f_2)] \tag{26}$$

where $R(f)$ is the Fourier transform of the random signal $R(nT)$, n is an integer index, T is the sampling interval, and $E[.]$ refers to nondeterministic signals (i.e., expectation operation).

Features are utilized in our work based on the integrated bispectrum along the dashed line with slope = r . The frequency (f) normalized by the Nyquist frequency to be between 0 and 1.

HOS will give information about signal wave shape. If there is no Bispectral associating, the bispectrum of a real signal is uniquely defined with the triangle:

$$0 \leq f_2 \leq f_1 \leq f_1 + f_2 \leq 1; \tag{27}$$

parameters are obtained by integrating along the straight lines passing through the origin in bifrequency space. The district of calculation and the line of integration are depicted in Figure 2.

In this work, we calculated these features within the region Ω .

(1) The Bispectral phase entropy (P_{he}):

$$P_{he} = \sum p(w_n) \log p(w_n) \tag{28}$$

(2) Bispectral entropy (P_1):

$$P_1 = - \sum_n p_i \log(p_i) \tag{29}$$

where $p_i = |B(f_1, f_2)| / \sum_{\Omega} |B(f_1, f_2)|$

Ω is the region as shown in Figure 2.

(3) Bispectral Squared Entropy (P_2):

$$P_2 = - \sum_n p_n \log(p_n) \tag{30}$$

where $p_n = |B(f_1, f_2)^2| / \sum_{\Omega} |B(f_1, f_2)^2|$

(4) Bispectral Cubic Entropy (P_3):

$$P_3 = - \sum_n p_q \log(p_q) \tag{31}$$

where $p_q = |B(f_1, f_2)^3| / \sum_{\Omega} |B(f_1, f_2)^3|$.

In our work, we have extracted the four bispectrum invariants, depicted over every radon-transformed thyroid nodule image.

2.3.3. Proposed System. The block diagram of the proposed system which is depicted in Figure 3. It is started with image preprocessing stage where the entire set of thyroid nodule images (Benign and malignant) is preprocessed by enhancing images visual contrast using neutrosophic based image enhancement followed by image sharpening technique to highlight images edges. Then image speckle noise reduction block using SRAD applied on visually enhanced ultrasound images. The images then are subdivided into equally sized nonoverlapped square blocks $B(m,n)$; then the 3rd order HOSE cumulants entropies at different angles are calculated after applying the Radon transform on the preprocessed ultrasound image blocks. The seed selection process is then started by constructing the entropies vector E_v for every image block which includes entropies values from different categories (Bispectral phase entropy (P_{he}), Bispectral Entropy (P_1), Bispectral Squared Entropy (P_2), and Bispectral Cubic Entropy (P_3)) at different angles ($0^\circ, 60^\circ, 120^\circ, 180^\circ$) within the range between maximum and average values calculated from all image blocks. The candidate block then is selected by considering the longest E_v vector: $\text{Max}(L(E_v))$, and hence the center of the candidate block is calculated and considered as a seed point. In the case of more than one candidate block (having E_v with the same length),

$$\begin{aligned} \text{Max}(L(E_{v_1})) &= \text{Max}(L(E_{v_2})) \\ &= \dots \text{Max}(L(E_{v_n})) \end{aligned} \tag{32}$$

The one with highest Structures Similarity Index (SSIM) is becoming the candidate block. The SSIM used for measuring the similarity between two images (or image blocks).

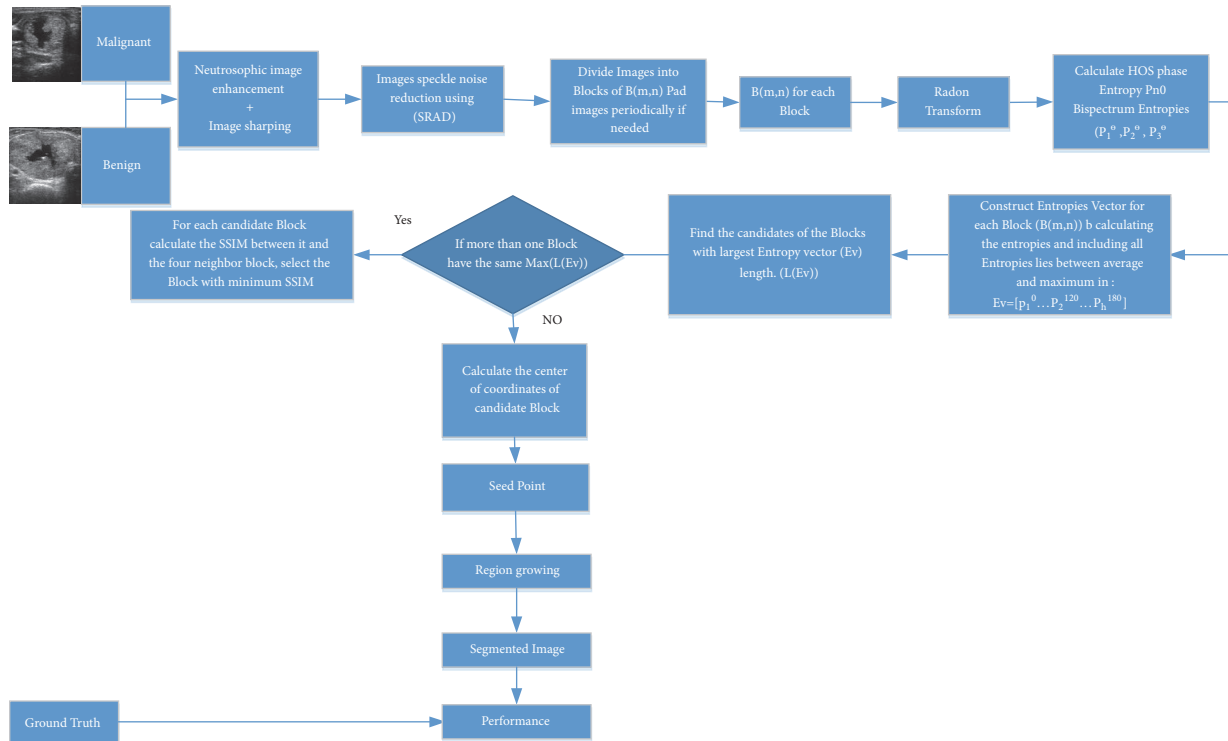


FIGURE 3: The flowchart of the proposed system.

TABLE 1: Depicts the five-selected images with their candidates block and blocks center.

Image name	Best Block	No. of Blocks	Block XY-Position	Center point(s)
12-malignant	237	18×31	(8,20)	(83,215)
22-benign	78	19×22	(4,12)	(39,127)
28-benign	(137, 187)	(19×25,19×25)	(6,12), (8,12)	(61,127), (83,127)
31- malignant	180	19×24	(10,9)	(105,94)
48-benign	302	17×28	(11,22)	(116,237)

The SSIM index is a full reference metric. Thus, if there is a higher amount of homogeneity between the candidate block and its neighbors block its center is selected as a seed. After seed selection, the region growing technique is applied to each thyroid nodule ultrasound images to extract the suspicious area. The ground truth manually segmented images by the specialist are compared with the automatically segmented images and, finally, a group of measurements was carried out to evaluate the output of the proposed system.

2.4. Performance Measures. In this work to explore the performance of segmentation methods, both area-based and boundary-based metrics have been utilized. Area based error metrics, True Positive (TP), False Positive (FP), and Dice Coefficient (DC) have been employed. The boundary-based error metrics, for example, Hausdorff Distance (HD), are utilized to decide the possible disagreement over two curves [39].

3. Results and Discussion

The proposed segmentation scheme is called seed selection based on higher order spectra (SSHOS). Five real thyroid ultrasound images from dataset are selected and displayed from the used dataset. All images have low contrast with weak boundaries between nodules and abutting tissues.

Table 2 shows the values of maximum SSIM calculated for the 4-neighbour blocks for the candidate blocks. It is clear that the image 28-benign has two candidate blocks (137,187) (see Table 1). The block numbered 187 is selected because it has higher SSIM as compared to the block 137. And this is obvious in Table 2. The Max Neighbor SSIM is calculated by summing out all 4- neighbor's SSIMs.

Figure 4(a) shows an original ultrasound image. Figure 4(b) demonstrates ground truth segmented image. Neutrosophic image enhancement and sharpening is introduced in Figure 4(c); Figure 4(d) represented despeckled image utilizing SRAD method. Figures 4(e) and 4(f) demonstrate the visual consequences of SSHOS and segmented sectioned utilizing region growing. It is additionally demonstrating

TABLE 2: The SSIM for the 4-neighbor blocks.

Image name	Max Neighbor SSIM	SSIM BLK1	SSIM BLK2	SSIM BLK3	SSIM BLK4
12-malignant	3.467184				
22-benign	1.64305				
28-benign	(0.9594,2.2008)	(0.0443,0.443)	(0.3386,0.5748)	(0.19089,0.55709)	(0.4742,0.62586)
31-malignant	2.160953				
48-benign	1.879466				

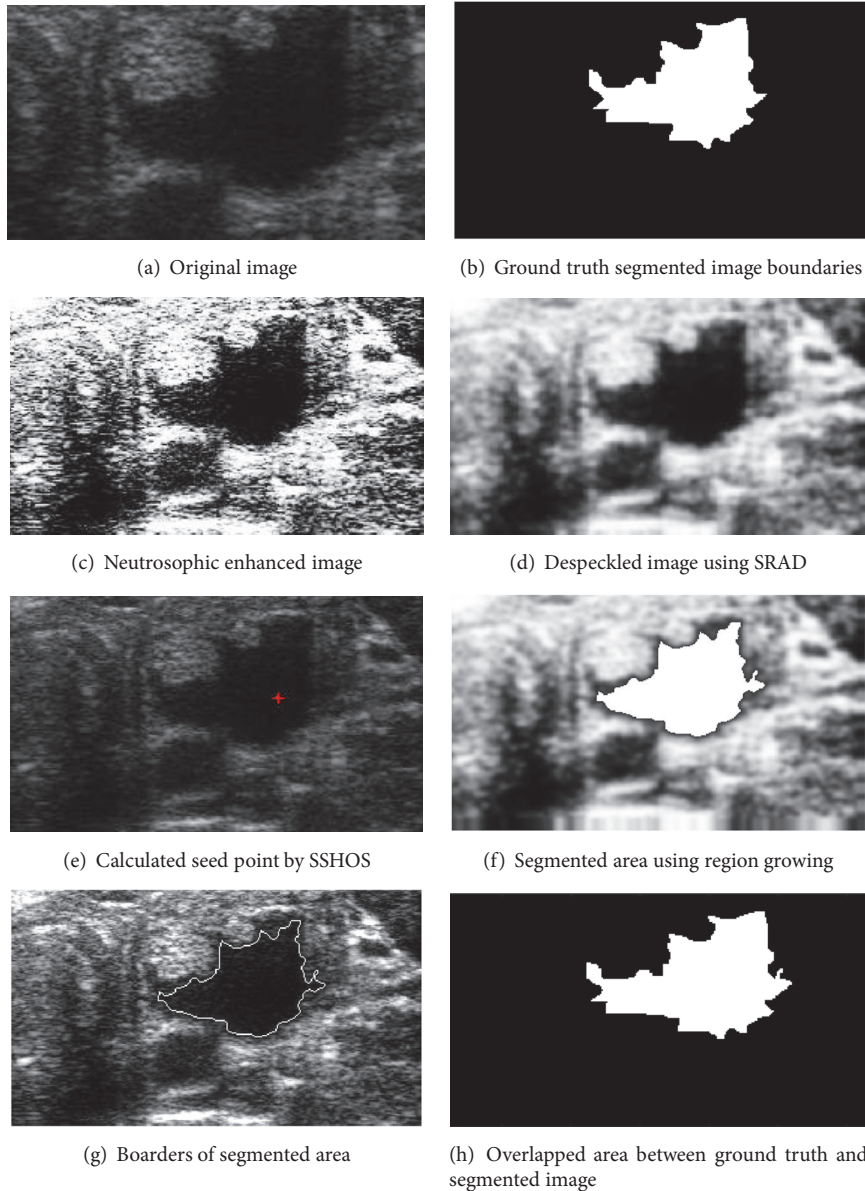


FIGURE 4: Ultrasound image (image 12 M).

that SSHOS can be utilized for accurate segmentation and separation of particular tissues. Figure 4(g) illustrated that the SSHOS can better preserved the nodule's boundaries in thyroid ultrasound image while overlapped area between ground truth and segmented image clearly showed up in

Figure 4(h). Figures 5–8 show the same details as presented by Figure 4 for the other images listed in Table 1.

Figures 9(a), 9(b), 9(c), and 9(d) show graphical illustration for the spectral entropies (P1, P2, P3, and Pph) at different angles for the image (12-malignant). It is clear that the values

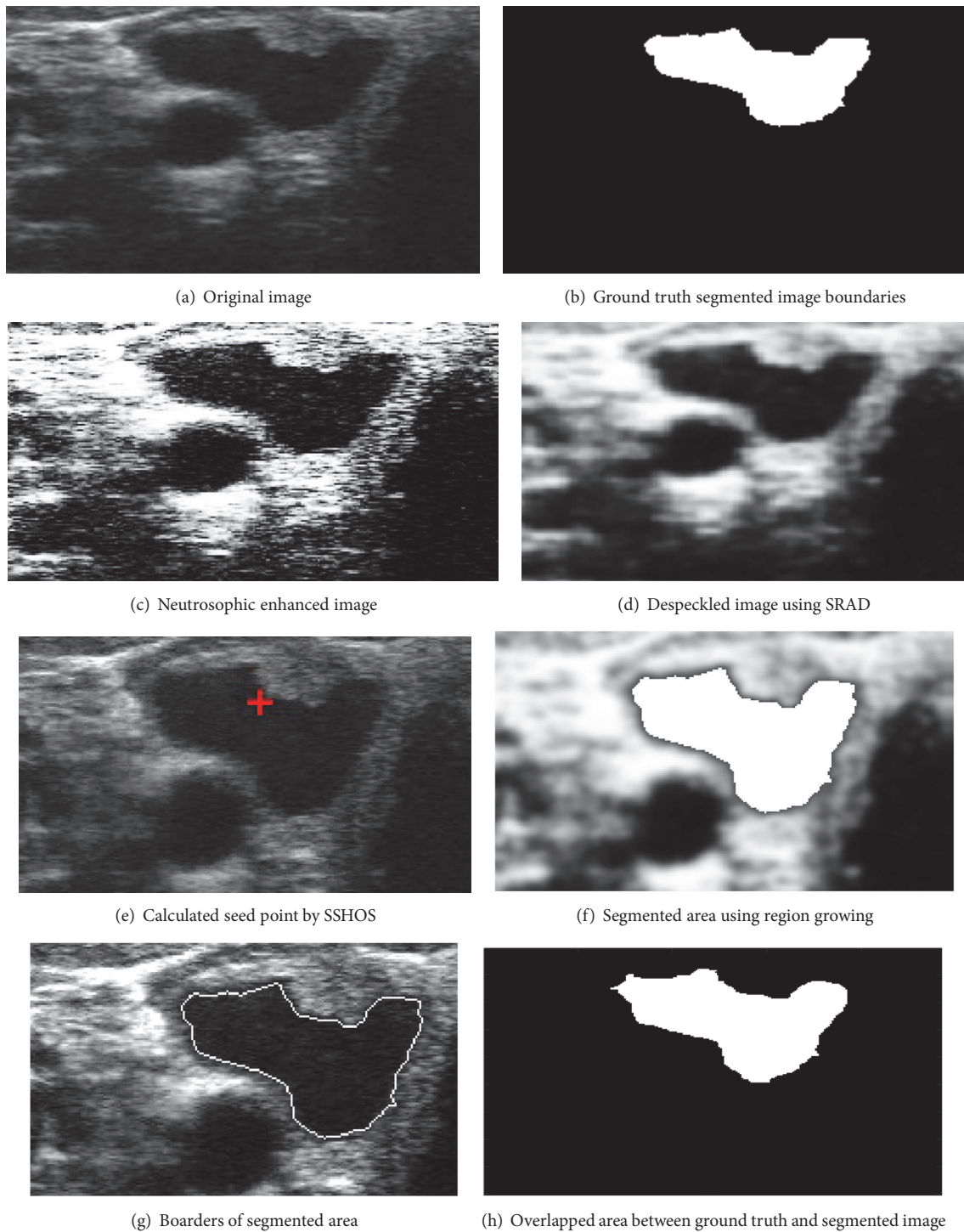


FIGURE 5: Ultrasound image (image 22B).

of different entropies at block numbered (237) are higher than the other blocks entropies. So it is selected as a candidate block automatically.

The performance of segmentation method has been compared with other methods which were applied on the same data set of thyroid ultrasound images as listed in Table 3. As apparent from results, it is seen that SSHOS

outperforms all other methods by accomplishing highest qualities regarding TP, SI. The larger estimations of area-based metrics created by SSHOS guarantee more similarity between the regions segmented by segmentation methods. The SSHOS uncovers a change in FP and HD when contrasted with different techniques. Moreover, smallest HD and FP determines the prevalence of proposed techniques as looked

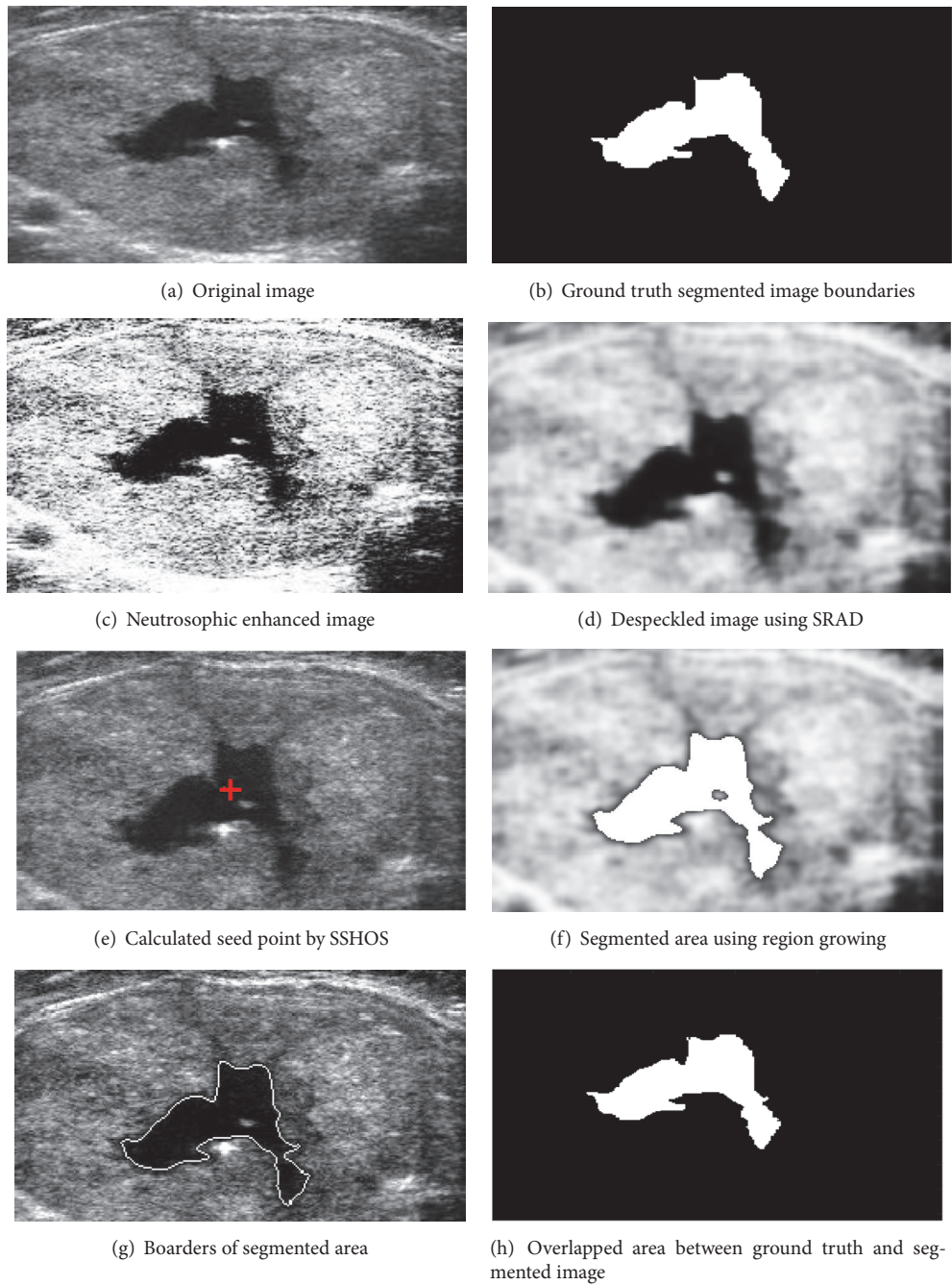


FIGURE 6: Ultrasound image (image 28B).

TABLE 3: Performance measures of segmentation method (SSHOS) of dataset.

Scheme Name	HD (Pixels)	TP (%)	FP (%)	SI (%)	Dice coefficient	Density	Area	density k	area k
SSHOS	0.42 ± 0.24	96.44 ± 3.01	3.55 ± 1.45	80.57 ± 1.06	92.24 ± 6.47	0.60 ± 0.17	3123 ± 950	0.60 ± 0.19	3627 ± 1313
Poonguzh et al. [21]	0.66 ± 0.22	93.51 ± 5.94	6.48 ± 3.94	67.85 ± 1.37	80.85 ± 9.04	0.97 ± 0.09	5122 ± 1049	0.80 ± 0.05	6727 ± 1787
Mohammed et al. [40]	0.68 ± 0.28	52.26 ± 4.71	47.73 ± 4.95	51.44 ± 3.01	67.93 ± 2.19	0.76 ± 0.01	4772 ± 699	0.611 ± 0.19	2570 ± 1378
NDRLS [5]	0.2 ± 0.82	95.4 ± 3.5	7.3 ± 5.3		94.2 ± 4.6				

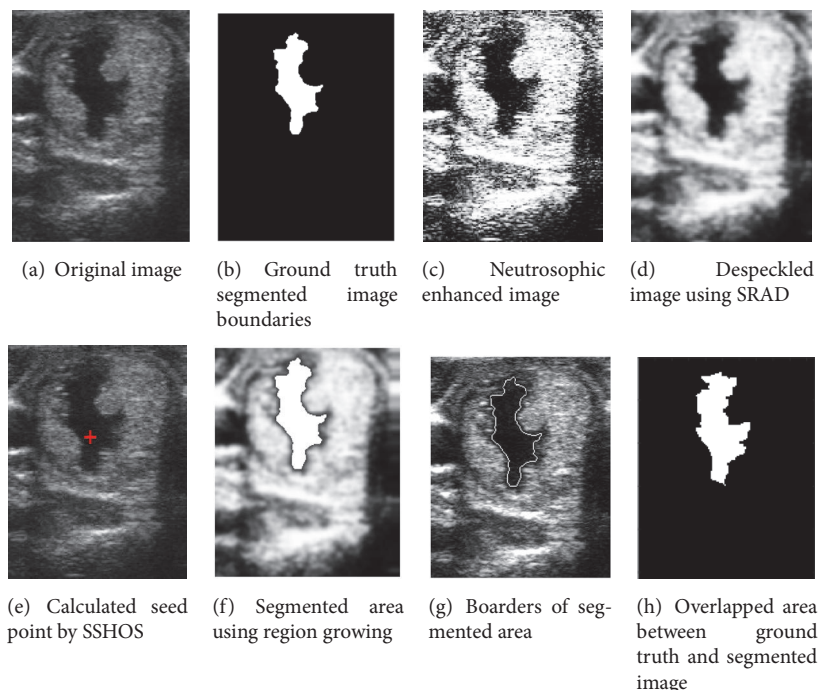


FIGURE 7: Ultrasound image (image 31M).

TABLE 4: Performance measures of segmentation method (SSHOS) with and without enhancement images.

Scheme Name	HD (Pixels)	TP (%)	FP (%)	SI (%)	Dice coefficient	density	area	density k	area k
SSHOS	0.42 ± 0.24	96.445 ± 3.01	3.55 ± 1.45	80.57 ± 1.06	92.24 ± 6.47	0.60 ± 0.17	3123 ± 950	0.6086 ± 0.195	3627 ± 1313
without neutrosophic enhancement	0.38 ± 0.12	95.82 ± 3.63	4.17 ± 3.12	72.06 ± 9.55	85.77 ± 6.11	0.69 ± 0.08	2466 ± 1607	0.68 ± 0.17	3175 ± 1765

at over different methods. The SSHOS is superior to the greater part of different techniques as far as FP, TP, DC, SI, and HD.

The performance of SSHOS with or without speckle reduction is additionally demonstrated by the boundary error measurements as well, which demonstrate that the forms created by SSHOS with or without speckle reduction are significantly nearer to the manual depictions as given in Table 5. As obvious from these outcomes, it is seen that SSHOS can be applied without speckle reduction for the nodule segmentation. All these results justify the great indeterminacy dealing with capacity of neutrosophic domain.

Furthermore, SSHOS can prevent leakage through weak edges resulting in exact extraction of nodule boundaries by dealing with the intensity in homogeneity well. The mean values of TP, FP, DC, SI, and HD acquired with SSHOS are ($96.44 \pm 3.01\%$), ($3.55 \pm 1.45\%$), ($92.24 \pm 6.47\%$), ($80.57 \pm 1.06\%$), and (0.42 ± 0.24 pixels). For the most part, SSHOS join to higher qualities than [21, 40].

Table 4 shows a comparison between the proposed method with and without neutrosophic enhancement. It is clear that a degradation in the TP, FP, SI, and all other measures.

Table 5 also shows a comparison between the proposed method (SSHOS) with and without speckle noise reduction. It is clear that the noise reduction technique (SRADA) improves system performance.

4. Conclusions

The goal of this study is to improve a robust algorithm for segmenting thyroid nodules on ultrasound image that is a unique challenge in ultrasound segmentation. The result showed that our algorithm is one of the best automatic segmentation methods for thyroid nodules on ultrasound images. In seed selection based on Higher Order Spectra (SSHOS), however, the initial contours are automatically identified very close to the actual thyroid gland nodule boundaries, which can be quickly refined by the level set. Experiments (SSHOS) are highly efficient, robust, and accurate. The experimental results show that SSHOS has better performance results as compared to other methods. It can also prevent border leakage into adjacent tissues and smooth the background.

SSHOS also needs no training and user input. In addition, despite intensity variations, the method can reveal thyroid nodule borders. The higher values of quality meters achieved

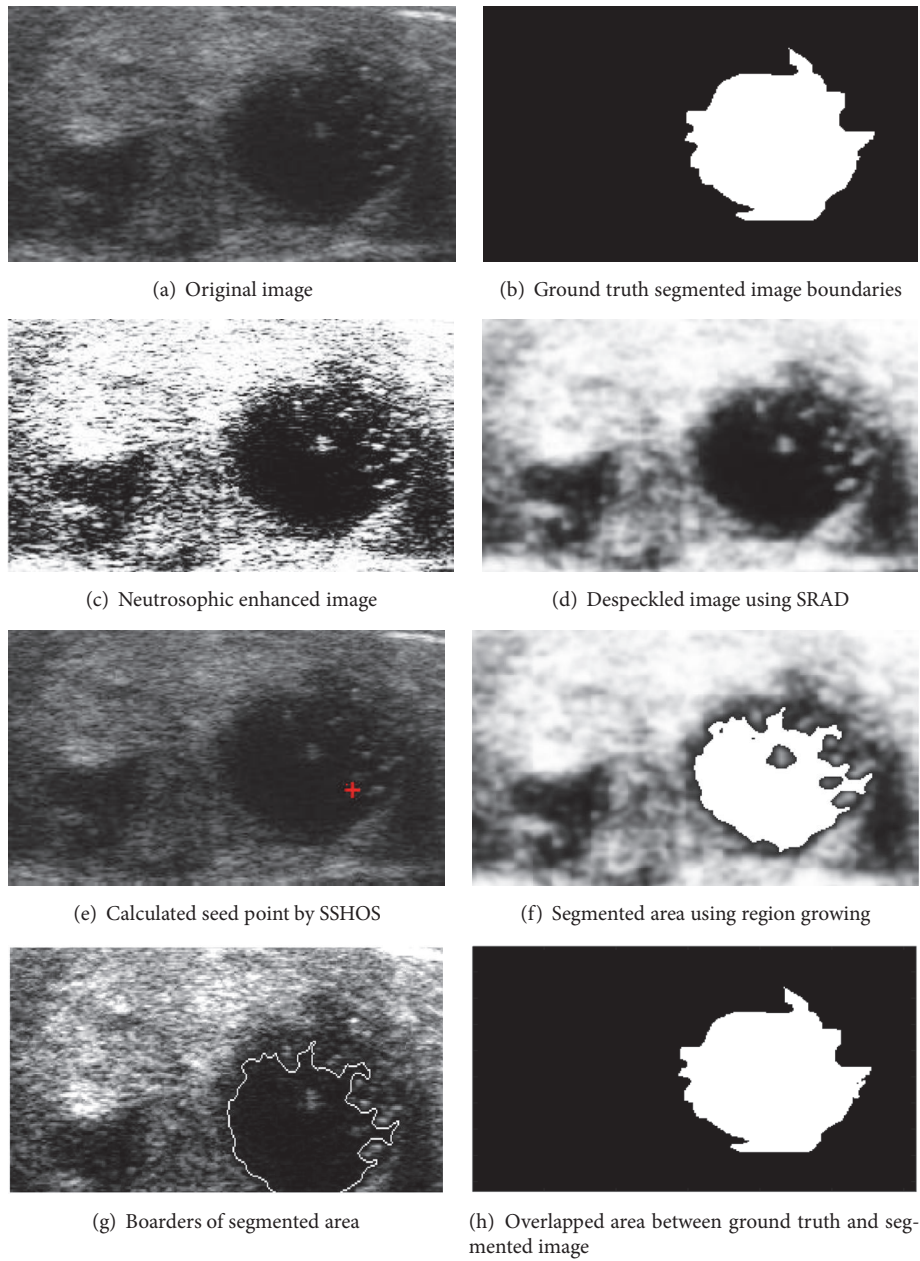


FIGURE 8: Ultrasound image (image 48B).

TABLE 5: Performance measures of segmentation method with and without speckle noise reduction.

Scheme Name	HD (Pixels)	TP (%)	FP (%)	SI (%)	Dice coefficient	Density	area	density k	area k
Without speckle reduction	0.51 ± 0.10	94.19 ± 5.25	5.80 ± 2.56	83.35 ± 1.71	87.92 ± 10.30	0.88 ± 0.10	5923 ± 1850	0.77 ± 0.25	6349 ± 1409
SSHOS	0.42 ± 0.24	96.44 ± 3.01	3.55 ± 1.45	80.57 ± 1.06	92.24 ± 6.47	0.60 ± 0.17	3123 ± 950	0.60 ± 0.19	3627 ± 1313

by the SSHOS method over other state-of-the-art methods are recommended in medical practice.

Thus, without any human intervention, a fully automated CADe system for segmenting nodules in thyroid ultrasound images was developed. It can be used as a

second tool for assisting endocrinologists in the automated and accurate delineation of thyroid nodules in ultrasound images. This helps reduce the number of false positives and improves accurate thyroid nodules detection.

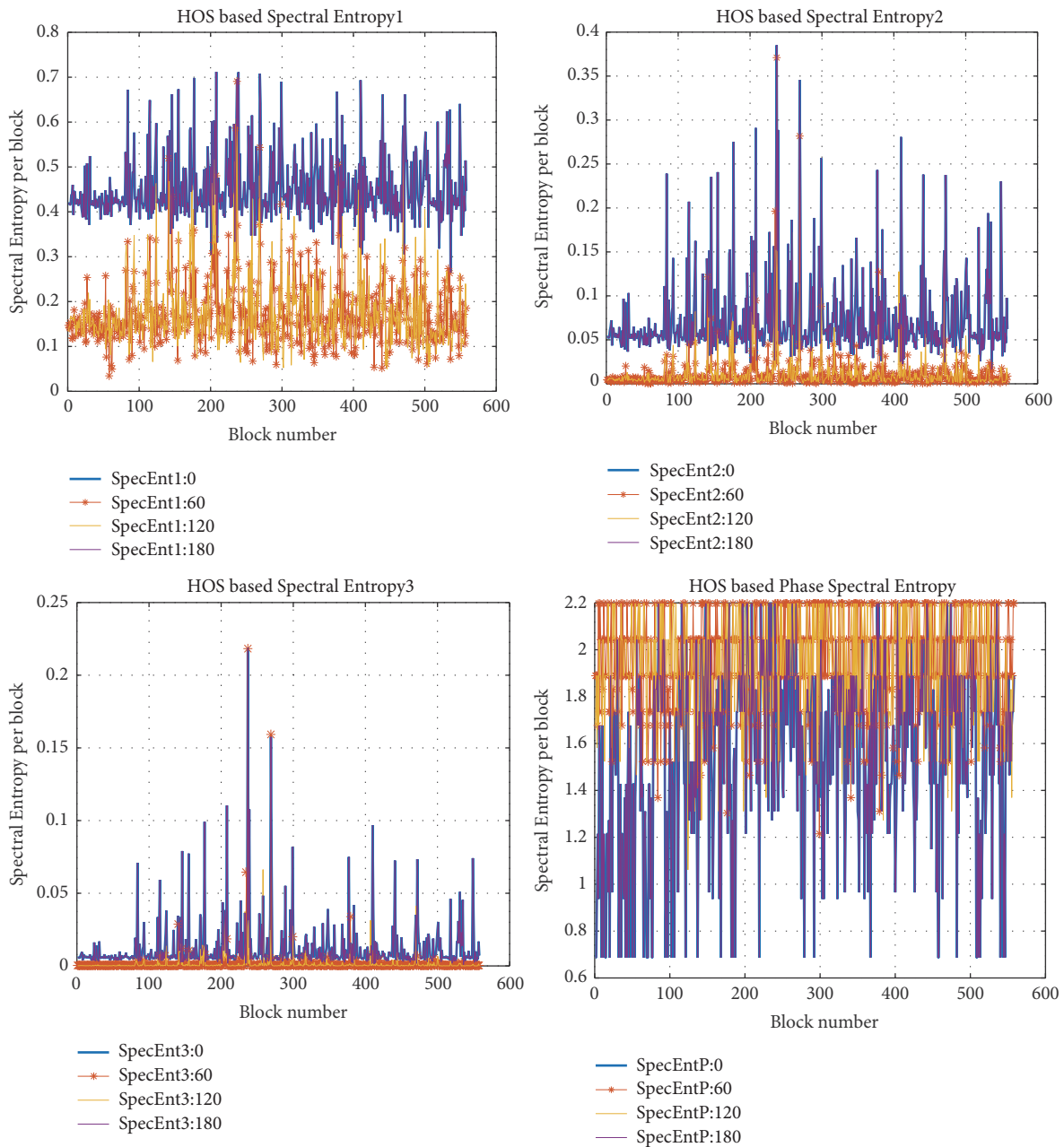


FIGURE 9: HOSE for different blocks and angles in image (12-malignant).

Further research may be extended to validate the proposed system for three-dimensional ultrasound images and Doppler ultrasound images, since this work deals only with B-mode ultrasound images. This system still needs to explore other imaging modalities.

Data Availability

We took all data (images) for both Benign and Malignant states in TDID (Thyroid DIGital Image database) which consists of a set of B-mode ultrasound images from the website of Computer Imaging & Medical Applications Laboratory, Universidad Nacional de Colombia Laboratory.

Conflicts of Interest

The authors declare that they have no conflicts of interest.

References

- [1] U. R. Acharya, P. Chowriappa, H. Fujita et al., "Thyroid lesion classification in 242 patient population using Gabor transform features from high resolution ultrasound images," *Knowledge-Based Systems*, vol. 107, pp. 235–245, 2016.
- [2] R. L. Siegel, K. D. Miller, and A. Jemal, "Cancer statistics," *CA: A Cancer Journal for Clinicians*, vol. 68, no. 1, pp. 7–30, 2018.

- [3] E. G. Keramidas, D. Maroulis, and D. K. Iakovidis, "TND: a thyroid nodule detection system for analysis of ultrasound images and videos," *Journal of Medical Systems*, vol. 36, no. 3, pp. 1271–1281, 2012.
- [4] D. Koundal, S. Gupta, and S. Singh, "Survey of computer-aided diagnosis of thyroid nodules in medical ultrasound images," in *Advances in Intelligent Systems and Computing*, vol. 177, pp. 459–467, Springer, 2013.
- [5] D. Koundal, S. Gupta, and S. Singh, "Computer aided thyroid nodule detection system using medical ultrasound images," *Biomedical Signal Processing and Control*, vol. 40, pp. 117–130, 2018.
- [6] N. Gupta, M. N. S. Swamy, and E. Plotkin, "Despeckling of medical ultrasound images using data and rate adaptive lossy compression," *IEEE Transactions on Medical Imaging*, vol. 24, no. 6, pp. 743–754, 2005.
- [7] S. T. Acton, "Deconvolutional speckle reducing anisotropic diffusion," in *Proceedings of the IEEE International Conference on Image Processing, ICIP 2005*, vol. 1, pp. 5–8, IEEE, Genova, Italy, 2005.
- [8] I. Avazpour, M. I. Saripan, A. J. Nordin, and R. S. A. R. Abdullah, "Segmentation of extrapulmonary tuberculosis infection using modified automatic seeded region growing," *Biological Procedures Online*, vol. 11, no. 1, pp. 241–252, 2009.
- [9] N. A. Mat Isa, S. Sabaruddin, U. K. Ngah, and K. Z. Zamli, "The potential use of modified seed-based region growing technique for automatic detection of breast microcalcifications and tumour areas," *Jurnal Teknologi*, vol. 44, no. D, pp. 151–164, 2006.
- [10] A. A. Salama, F. Smarandache, and M. Eisa, "Introduction to image processing via neutrosophic techniques," *Neutrosophic Sets and Systems*, vol. 5, pp. 59–64, 2014.
- [11] Y. Guo and H. D. Cheng, "New neutrosophic approach to image segmentation," *Pattern Recognition*, vol. 42, no. 5, pp. 587–595, 2009.
- [12] Y. Guo, H. D. Cheng, J. Tian, and Y. Zhang, "A novel approach to speckle reduction in ultrasound imaging," *Ultrasound in Medicine & Biology*, vol. 35, no. 4, pp. 628–640, 2009.
- [13] E. Karabatak, Y. Guo, and A. Sengur, "Modified neutrosophic approach to color image segmentation," *Journal of Electronic Imaging*, vol. 22, no. 1, p. 013005, 2013.
- [14] K. C. Chua, V. Chandran, U. R. Acharya, and C. M. Lim, "Application of higher order statistics/spectra in biomedical signals—a review," *Medical Engineering & Physics*, vol. 32, no. 7, pp. 679–689, 2010.
- [15] V. Chandran and S. L. Elgar, "Pattern recognition using invariants defined from higher order spectra—one-dimensional inputs," *IEEE Transactions on Signal Processing*, vol. 41, no. 1, pp. 205–211, 1993.
- [16] A. El-Jaroudi, T. Akgul, and M. Simaan, "Application of higher order spectra to multi-scale deconvolution of sensor array signals," in *Proceedings of the IEEE International Conference on Acoustics, Speech and Signal Processing, ICASSP '94*, pp. 413–416, Adelaide, Australia, 1994.
- [17] U. R. Abeyratne, A. P. Petropulu, and J. M. Reid, "Higher order spectra based deconvolution of ultrasound images," *IEEE Transactions on Ultrasonics, Ferroelectrics and Frequency Control*, vol. 42, no. 6, pp. 1064–1075, 1995.
- [18] R. S. M. Khan, "Image segmentation methods: a comparative study," *International Journal of Soft Computing and Engineering*, vol. 3, no. 4, 2013.
- [19] G. Li and Y. Wan, "Adaptive seeded region growing for image segmentation based on edge detection, texture extraction and cloud model," in *Proceedings of the First International Conference on Information Computing and Applications, ICICA'10*, vol. 6377, pp. 285–292, Springer-Verlag, 2010.
- [20] B. Senthilkumar, G. Umamaheswari, and J. Karthik, "A novel region growing segmentation algorithm for the detection of breast cancer," in *Proceedings of the 2010 IEEE International Conference on Computational Intelligence and Computing Research, ICCIC 2010*, pp. 38–41, 2010.
- [21] S. Poonguzhali and G. Ravindran, "A complete automatic region growing method for segmentation of masses on ultrasound images," in *Proceedings of the 2006 International Conference on Biomedical and Pharmaceutical Engineering, ICBPE 2006*, pp. 88–92, 2006.
- [22] F. Deboeverie and F. Deboeverie, "Image segmentation with adaptive region growing based on a polynomial surface model based on a polynomial surface model," *Journal of Electronic Imaging*, vol. 22, no. 4, 2013.
- [23] S. Michahial, B. Thomas, and S. Kiran, "A novel algorithm to select a seed point automatically in breast ultrasound image," *Indian Journal of Science and Technology*, vol. 10, no. 1, pp. 1–8, 2017.
- [24] Y.-L. Chang and X. Li, "Adaptive image region-growing," *IEEE Transactions on Image Processing*, vol. 3, no. 6, pp. 868–872, 1994.
- [25] N. Mohd Saad, S. A. R. Abu-Bakar, S. Muda, M. Mokji, and A. R. Abdullah, "Fully automated region growing segmentation of brain lesion in diffusion-weighted MRI," *IAENG International Journal of Computer Science (IJCS)*, vol. 39, no. 2, pp. 155–164, 2012.
- [26] A. Q. Al-Faris, U. K. Ngah, N. A. M. Isa, and I. L. Shuaib, "Computer-aided segmentation system for breast MRI tumour using modified automatic seeded region growing (BMRI-MASRG)," *Journal of Digital Imaging*, vol. 27, no. 1, pp. 133–144, 2014.
- [27] M. A. Alattar, N. F. Osman, and A. S. Fahmy, "Myocardial segmentation using constrained multi-seeded region growing," in *Proceedings of the International Conference Image Analysis and Recognition, ICIAR 2010, Part II*, vol. 6112 of *Lecture Notes in Computer Science*, pp. 89–98, 2010.
- [28] L. Pedraza, C. Vargas, F. Narváez, O. Durán, E. Muñoz, and E. Romero, "An open access thyroid ultrasound-image database," in *Proceedings of the 10th International Symposium on Medical Information Processing and Analysis*, vol. 9287, Cartagena de Indias, Colombia, 2015.
- [29] X. Su, W. Fang, Q. Shen, and X. Hao, "An image enhancement method using the quantum-behaved particle swarm optimization with an adaptive strategy," *Mathematical Problems in Engineering*, vol. 2013, Article ID 824787, 14 pages, 2013.
- [30] F. Samarandache, "A unifying field in logics neutrosophic logic," in *Neutrosophy, Neutrosophic Set, Neutrosophic Probability*, American Research Press, Rehoboth, Del, USA, 3rd edition, 2003.
- [31] J. Shan, H. D. Cheng, and Y. Wang, "A novel segmentation method for breast ultrasound images based on neutrosophic l-means clustering," *Medical Physics*, vol. 39, no. 9, pp. 5669–5682, 2012.
- [32] H. D. Cheng and J.-R. Chen, "Automatically determine the membership function based on the maximum entropy principle," *Information Sciences*, vol. 96, no. 3-4, pp. 163–182, 1997.

- [33] H. D. Cheng, J. Wang, and X. Shi, "Microcalcification detection using fuzzy logic and scale space approaches," *Pattern Recognition*, vol. 37, no. 2, pp. 363–375, 2004.
- [34] H. D. Cheng and J. Li, "Fuzzy homogeneity and scale-space approach to color image segmentation," *Pattern Recognition*, vol. 36, no. 7, pp. 1545–1562, 2003.
- [35] H. D. Cheng and H. Xu, "A novel fuzzy logic approach to contrast enhancement," *Pattern Recognition*, vol. 33, no. 5, pp. 809–819, 2000.
- [36] R. C. Gonzalez and R. E. Woods, *Digital Image Processing*, NJ, USA, 2nd edition, 1987.
- [37] U. R. Acharya, C. K. Chua, E. Y. K. Ng, W. Yu, and C. Chee, "Application of higher order spectra for the identification of diabetes retinopathy stages," *Journal of Medical Systems*, vol. 32, no. 6, pp. 481–488, 2008.
- [38] A. P. Petropulu, "Higher-order spectra in biomedical signal processing," *IFAC Proceedings Volumes*, vol. 27, no. 1, pp. 47–52, 1994.
- [39] R.-F. Chang, W.-J. Wu, W. K. Moon, and D.-R. Chen, "Automatic ultrasound segmentation and morphology based diagnosis of solid breast tumors," *Breast Cancer Research and Treatment*, vol. 89, no. 2, pp. 179–185, 2005.
- [40] M. M. Abdelsamea, G. Gnecco, and M. M. Gaber, "A SOM-based Chan-Vese model for unsupervised image segmentation," *Soft Computing*, vol. 21, no. 8, pp. 2047–2067, 2017.